



Original Article

Evolving antiferroelectric stability and phase transition behavior in $\text{NaNbO}_3\text{-BaZrO}_3\text{-CaZrO}_3$ lead-free ceramics

He Qi, Ruzhong Zuo*

Institute of Electro Ceramics & Devices, School of Materials Science and Engineering, Hefei University of Technology, Hefei, 230009, PR China



ARTICLE INFO

Keywords:
Antiferroelectricity
 NaNbO_3
Lead-free ceramics
Phase transition

ABSTRACT

The stability of antiferroelectricity in NaNbO_3 ceramics was found to evolve with co-doping x mol% CaZrO_3 and 6 mol% BaZrO_3 , from a dominant ferroelectric (FE) orthorhombic Q phase ($x = 0$) to a gradually stabilized antiferroelectric (AFE) orthorhombic P phase owing to different ionic radii of Ba and Ca ions. Although a complete AFE P phase appears at $x = 0.5$, the field induced AFE-FE phase transformation is irreversible at first, and then becomes partially reversible at $x = 1$ and finally completely reversible at $x = 3$. The above-mentioned change process proves to be associated with the enhancing stability of antiferroelectricity with x , as evidenced by means of dielectric, polarization and strain properties as well as in/ex-situ synchrotron x-ray diffraction and Raman spectra. A composition-field phase diagram for the NN-based lead-free AFE ceramic was constructed on basis of the phase structural change, which would provide a clear understanding of how ion doping influences its antiferroelectricity.

1. Introduction

Antiferroelectric (AFE) materials have attracted much attention owing to their enigmatic structures and excellent electromechanical properties [1]. Chains of ions in the AFE crystal are spontaneously polarized, but with neighboring chains polarized in antiparallel directions [2,3]. As a result, there is macroscopically no net spontaneous polarization or the piezoelectric effect. When an external electric field is applied, the antiparallel dipoles can be flipped and forced to be parallel, corresponding to an electric field-induced AFE to ferroelectric (FE) phase transition. A series of interesting properties accompanied by the phase transition provide the physical foundation for important engineering applications of AFE materials in digital displacement transducers, energy storage capacitors, electrocaloric cooling devices, flat panel displays and so on [1,4–6].

NaNbO_3 (NN) is a well-documented AFE perovskite compound with an orthorhombic Pbma (P phase) space group at room temperature (RT) [7,8]. It has attracted a lot of attention in recent years owing to its complex phase structure transition and the possibility of being lead-free FE or AFE candidates [9–12]. Particularly, stable antiferroelectricity was only detected in high-quality NN single crystals along the orthorhombic c axis [13]. However, coexisting AFE orthorhombic P phase and FE orthorhombic Q phase (space group $\text{P2}_1\text{ma}$) in NN at RT tend to transform into an FE phase by various means [14–16] owing to their

similar free energies, causing a square P-E hysteresis loop [17–20]. Therefore, how to effectively stabilize the antiferroelectricity in NN ceramics becomes a critical issue. So far a repeatedly achievable large strain from field induced AFE to FE phase transition has not yet been realized in NN-based AFE ceramics, as we observed in some conventional Pb-based AFE ceramics. A couple of research work was reported on attempting to enhance the AFE stability from the crystallographic point of view [21–25], among which various zirconates with lower tolerance factors were found to help stabilize the antiferroelectricity, as manifested by a few structural characterization techniques [22–25].

Our previous work indicated that the addition of a few amount of BaZrO_3 (BZ) can induce a series of phase structural transition in NN ceramics, accompanying interesting field induced strain characteristics [26]. In this work, on the basis of 6 mol% BZ, CaZrO_3 (CZ) was further introduced into NN ceramics to tune polar ordering through changing the tolerance factor of the unit cell owing to their different ionic radii. The evolution of AFE stability was specially explored by means of the observation of dielectric, polarization and strain properties as well as in/ex-situ synchrotron x-ray diffraction (XRD) and Raman spectra.

2. Experimental

The $(0.94-x)\text{NN}-0.06\text{BZ}-x\text{CZ}$ solid solution ceramics were prepared by a traditional mixed-oxide route. The raw chemicals of Na_2CO_3 ,

* Corresponding author.

E-mail address: piezolab@hfut.edu.cn (R. Zuo).

BaCO₃, CaCO₃, Nb₂O₅ and ZrO₂ (AR, Sinopharm Chemical Reagent Co., Ltd., CN) were mixed in stoichiometric ratio using stabilized zirconia balls in ethanol for 12 h. The dried powder mixture was calcined at 900 °C for 3 h. Followed by a grinding process in a planetary mill for 10 h, the powder was granulated using 5 wt% polyvinyl alcohol as the binder, and then uniaxially pressed into discs with a diameter of 10 mm and a thickness of ~0.5 mm. The sintering of samples was performed in the temperature range of 1350–1380 °C for 2 h after burning out the binder at 550 °C for 4 h. After the as-sintered sample discs were polished into a thickness of ~0.3 mm, two major surfaces were covered with silver paste with a little margin on the one side and then fired at 550 °C for 30 min. The compositions with $0 \leq x \leq 0.01$ and $0.02 \leq x \leq 0.03$ were poled at RT under a dc field of 15 kV/mm and 20 kV/mm for 15 min, respectively.

The grain morphology of the sintered samples was observed using a field-emission scanning electron microscope (FE-SEM, JEOL JSM-6490LV, Tokyo, Japan). Before the SEM observation, the sample was polished and thermally etched at 1200 °C for 30 min. The phase structure was analyzed by a conventional powder x-ray diffractometer (X'Pert-Pro MPD, Malvern Panalytical, Netherlands) with Cu K α radiation. The full XRD data were analyzed by the Rietveld refinement using GSAS software. Raman spectra were collected at RT on well-polished pellets by 532-nm excitation using a Raman spectrometer (LabRam HR Evolution, HORIBA JOBIN YVON, Longjumeau Cedex, France). Dielectric properties were measured as a function of temperature and frequency using an LCR meter (Agilent E4980 A, Santa Clara, CA) at a heating rate of 180 °C/h. The quasi-static d_{33} of the samples was measured using a Berlincourt-meter (YE2703 A, Sinocera, Yangzhou, China). A ferroelectric test system (Precision LC, Radiant Technologies, Inc. Albuquerque, NM) was used to measure polarization versus electric field (P-E) and strain versus electric field (S-E) loops. Synchrotron XRD measurement was carried out on well-polished and Pt-sputtered disk samples under various electric field conditions at Shanghai Synchrotron Radiation Facility (SSRF) using beam line 14B1 ($\lambda = 1.2378 \text{ \AA}$) in a symmetric reflection geometry. Measurements were performed by high-resolution θ - 2θ step-scans using a Huber 5021 six-circle diffractometer with a NaI scintillation detector.

3. Results and discussion

Fig. 1 shows the grain morphology of a few (0.94- x)NN-0.06BZ- x CZ ceramics as sintered at their optimal temperatures ($x = 0$: 1375 °C; $x = 0.01$: 1370 °C; $x = 0.02$: 1365 °C; $x = 0.03$: 1360 °C). All samples exhibit dense and uniform microstructure with a relative density of over 96%. With the substitution of CZ for NN, the grain size of the sintered ceramic was found to slightly decrease from ~5 μm at $x = 0$ to ~3 μm at $x = 0.03$ probably because of slightly decreased sintering temperature.

Fig. 2(a) shows synchrotron XRD patterns of (100)_C, (110)_C, (200)_C and (220)_C diffraction peaks of the as-sintered (0.94- x)NN-0.06BZ- x CZ ceramics. All the studied compositions exhibit an orthorhombic phase at RT. Close examination on the peaks at 36.5° and 55° by means of

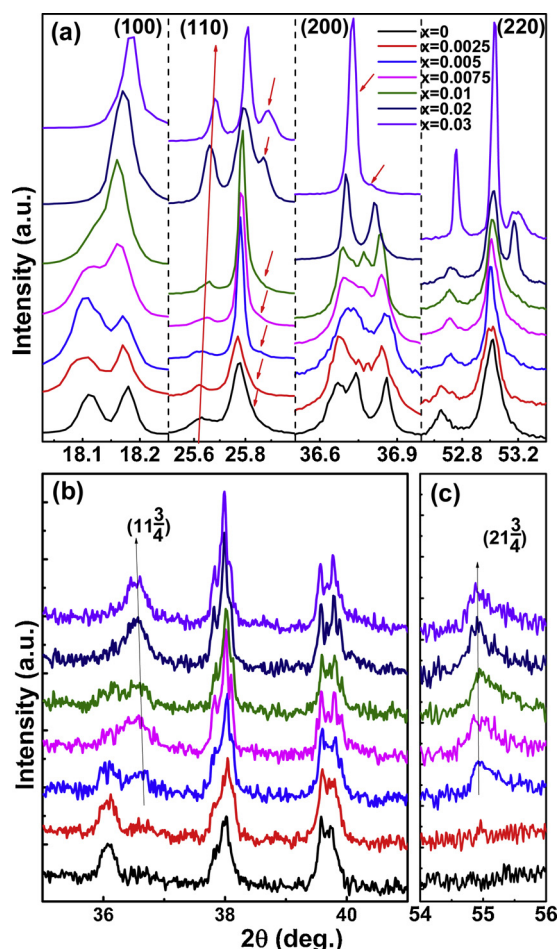


Fig. 2. XRD spectra of (0.94- x)NN-0.06BZ- x CZ ceramics: (a) synchrotron XRD results of several selected diffraction peaks, and the close view of (b) $\{1\ 1\ 3/4\}$ and (c) $\{2\ 1\ 3/4\}$ AFE superlattice peaks by means of conventional XRD.

conventional XRD, which are indexed as $\{1\ 1\ 3/4\}$ and $\{2\ 1\ 3/4\}$ superlattice peaks of AFE orthorhombic P phase of NN, respectively, [27] indicates the existence of a phase transformation in the studied composition range, as clearly seen in Fig. 2(b) and (c). These two superlattice peaks can be hardly detected in the 0.94NN-0.06BZ ($x = 0$) ceramic, suggesting that it mainly belongs to an FE orthorhombic phase. With the substitution of CZ for NN, both superlattice peaks start to appear and increase in intensities monotonously. Obvious features of the AFE P phase can be seen in the compositions of $x \geq 0.005$. A phase boundary between AFE and FE phases can be obtained close to the composition of $x = 0.0025$.

The Rietveld refinement on full profiles of conventional XRD patterns using GSAS software was carried out to further quantitatively analyze the phase structure, as shown in Fig. 3 for a few selected (0.94-

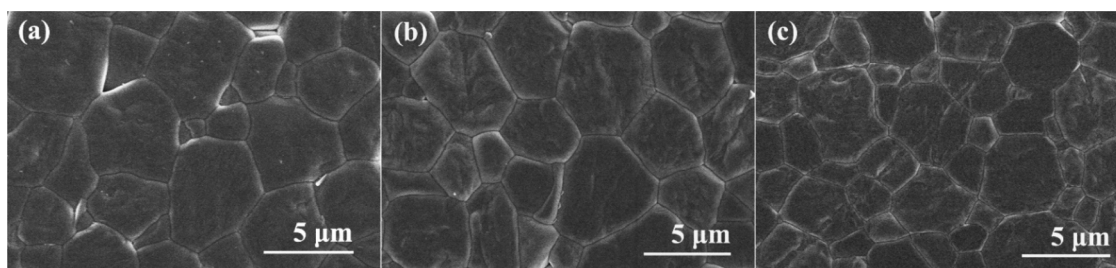


Fig. 1. SEM micrographs on polished and thermally etched surfaces of (0.94- x)NN-0.06BZ- x CZ ceramics sintered at their optimum temperatures: (a) $x = 0$, (b) $x = 0.01$ and (c) $x = 0.03$.

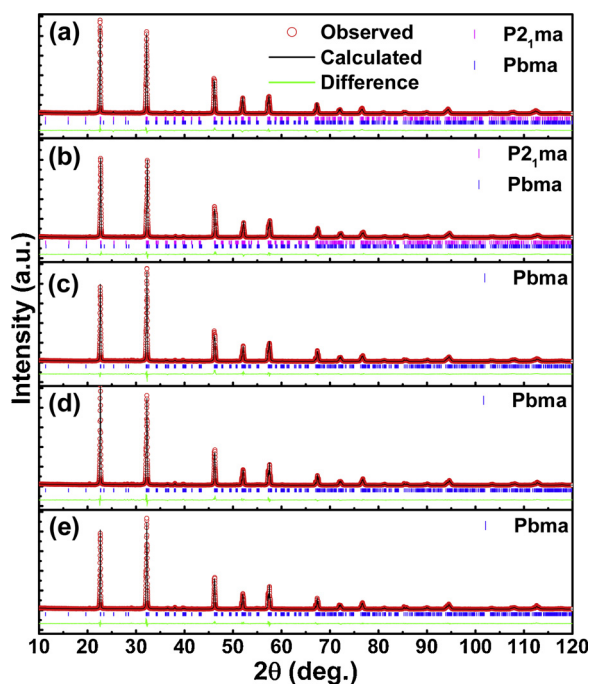


Fig. 3. Rietveld refinement plots of conventional XRD for a few selected (0.94-x)NN-0.06BZ-xCZ compositions: (a) $x = 0$, (b) $x = 0.0025$, (c) $x = 0.005$, (d) $x = 0.02$ and (e) $x = 0.03$.

x)NN-0.06BZ-xCZ samples. AFE orthorhombic P phase and FE orthorhombic Q phase are described as $Pbma$ and $P2_1ma$ space groups, respectively. [17,28,29] The refined structure parameters and various agreement factors are listed in Table 1, indicating that the fit between the observed and calculated profiles is satisfactory. The $x = 0$ sample was identified to be a dominant FE orthorhombic phase in addition to a slight amount of AFE P phase. With increasing CZ content, the content of the FE orthorhombic $P2_1ma$ phase decreases while the fraction of the AFE orthorhombic $Pbma$ phase increases monotonously. A pure AFE orthorhombic $Pbma$ phase can be achieved in the composition range of $x \geq 0.005$.

Raman is an effective method to reveal the AFE to FE phase transformation in NN-based perovskites as there exist obvious differences in the Raman active modes between $Pbma$ and $P2_1ma$ [17,29]. The AFE orthorhombic $Pbma$ symmetry with unit cell dimensions $\sqrt{2}a_p \times \sqrt{2}a_p \times 4a_p$ (with respect to the cubic perovskite with a lattice parameter a_p) has eight formula units ($Z = 8$, total 40 atoms) and total 117 possible optical modes according to the group theory analysis: $\Gamma_{opt} = 15A_g(R) + 17B_{1g}(R) + 15B_{2g}(R) + 13B_{3g}(R) + 13A_u(-) + 14B_{1u}(IR) + 16B_{2u}(IR) + 14B_{3u}(IR)$. The FE orthorhombic $P2_1ma$ symmetry with unit cell dimensions $\sqrt{2}a_p \times \sqrt{2}a_p \times 2a_p$ has four formula units ($Z = 4$). It should have total 57 possible optical modes: $\Gamma_{opt} = 16A_1(IR,R) + 13A_2(R) + 12B_1(IR,R) + 16B_2(IR,R)$. The evolution of Raman spectra

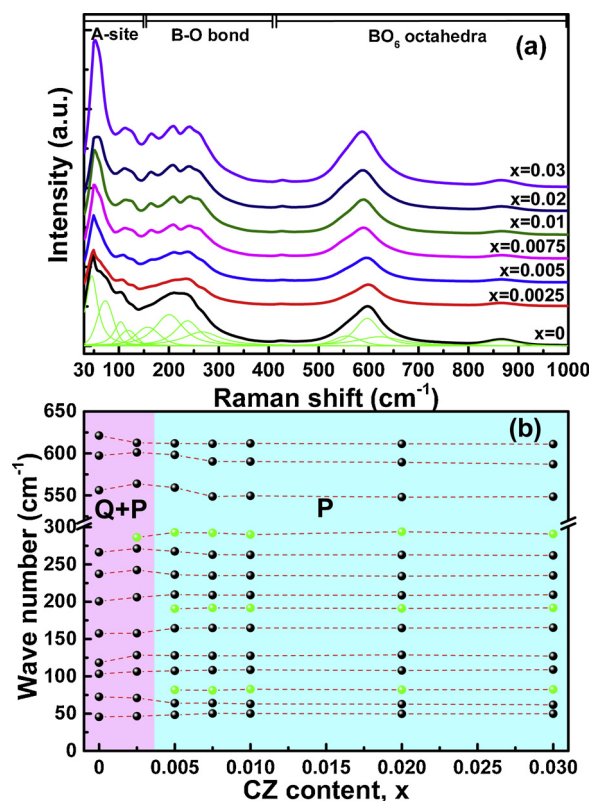


Fig. 4. (a) Raman spectra at RT of (0.94-x)NN-0.06BZ-xCZ samples together with a representative spectral deconvolution into Gaussian-Lorentzian-shape peaks using the $x = 0$ sample as an example, and (b) the wave-number variation of Raman peaks for different compositions.

collected at ambient condition in the range of $30\text{--}1000\text{ cm}^{-1}$ with changing CZ content is shown in Fig. 4(a). After the spectral deconvolution into Gaussian-Lorentzian-shape peaks, the composition dependence of the wave number of all well-defined Raman peaks is shown in Fig. 4(b). Very weak and poorly-defined peaks around 420 cm^{-1} and 870 cm^{-1} were not included. Obvious changes of Raman spectra associated with the structure transformation can be observed in the composition range of $0 \leq x \leq 0.005$. For the $x = 0$ composition, the Raman response below 400 cm^{-1} is obviously similar to that of NN-based FE Q phase instead of AFE P phase [17,29]. With increasing CZ content from $x = 0$ to above $x = 0.005$, distinct splitting of the Raman peaks can be observed around 89 cm^{-1} , 190 cm^{-1} and 290 cm^{-1} , as marked by green dots in Fig. 4(b). Simultaneously, the high-frequency B–O stretching bands around 600 cm^{-1} tends to shift to lower frequency with increasing CZ content. All the above phenomena are associated with the FE Q to AFE P phase transformation in the composition range of $0\text{--}0.005$ because of the softening of the stretching vibration caused by the off-center displacement of the Nb ions. The off-

Table 1

Refined structural parameters by using the Rietveld method for a few selected (0.94-x)NN-0.06BZ-xCZ ceramics.

x	Space group	Volume fraction	Lattice parameters	V (Å ³)	R _{wp} (%)	R _p (%)	χ ²
0	$P2_1ma$	92%	$a = 5.5912(1)\text{ \AA}$, $b = 7.8450(1)\text{ \AA}$, $c = 5.5459(1)\text{ \AA}$, $\alpha = \beta = \gamma = 90^\circ$	243.263(1)	7.77	5.93	2.76
	$Pbma$	8%	$a = 5.5901(3)\text{ \AA}$, $b = 15.6889(8)\text{ \AA}$, $c = 5.5491(4)\text{ \AA}$, $\alpha = \beta = \gamma = 90^\circ$	486.674(5)			
0.0025	$P2_1ma$	38%	$a = 5.5969(9)\text{ \AA}$, $b = 7.8607(4)\text{ \AA}$, $c = 5.5267(8)\text{ \AA}$, $\alpha = \beta = \gamma = 90^\circ$	243.199(7)	7.38	5.36	2.50
	$Pbma$	62%	$a = 5.5891(1)\text{ \AA}$, $b = 15.6869(2)\text{ \AA}$, $c = 5.5469(1)\text{ \AA}$, $\alpha = \beta = \gamma = 90^\circ$	486.407(2)			
0.005	$Pbma$	100%	$a = 5.5874(1)\text{ \AA}$, $b = 15.6866(2)\text{ \AA}$, $c = 5.5451(1)\text{ \AA}$, $\alpha = \beta = \gamma = 90^\circ$	486.020(2)	7.22	5.60	2.67
0.02	$Pbma$	100%	$a = 5.5847(1)\text{ \AA}$, $b = 15.6969(1)\text{ \AA}$, $c = 5.5406(1)\text{ \AA}$, $\alpha = \beta = \gamma = 90^\circ$	485.713(2)	6.83	5.12	1.94
0.03	$Pbma$	100%	$a = 5.5841(1)\text{ \AA}$, $b = 15.6801(2)\text{ \AA}$, $c = 5.5436(1)\text{ \AA}$, $\alpha = \beta = \gamma = 90^\circ$	485.411(2)	6.80	5.06	1.54

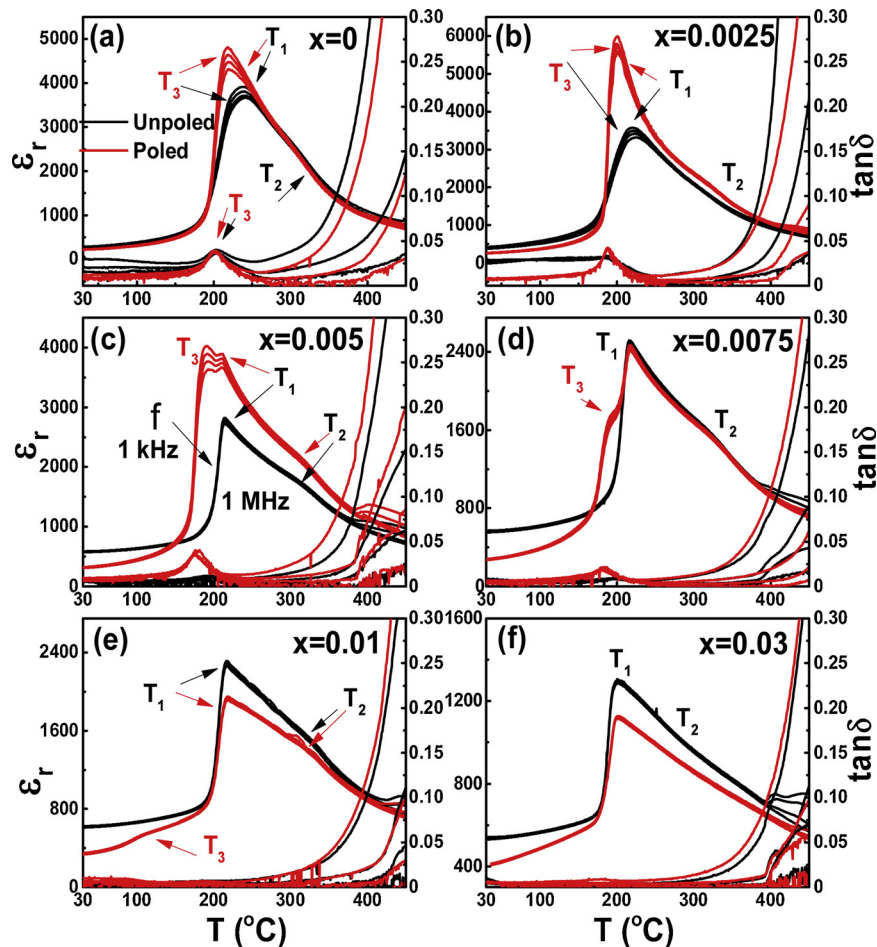


Fig. 5. Dielectric permittivity and loss tangent of poled and unpoled (0.94-x)NN-0.06BZ-xCZ ceramics as a function of temperature and frequency (1 kHz-1 MHz).

center displacement of Nb in Q phase is nearly symmetrical, while the displacement of Nb in P phase leads to the formation of two short and two long Nb–O bonds approximately in the (010) plane, resulting in more peaks on Raman spectra of the P phase [7].

Fig. 5 shows the dielectric permittivity (ϵ_r) and loss tangent ($\tan\delta$) as a function of temperature and frequency for poled and unpoled (0.94-x)NN-0.06BZ-xCZ ceramics. For the $x = 0$ virgin sample, it shows a dominant FE Q phase at RT before poling. A wide dielectric peak around 250 °C actually includes two peaks T_3 and T_1 , corresponding to the FE orthorhombic Q phase to AFE orthorhombic P phase transition and the AFE orthorhombic P to R phase (Pmnm space group) transition, respectively. Another dielectric anomaly above T_1 and T_3 (labeled as T_2) was believed to correlate with the phase transition from AFE orthorhombic R phase to paraelectric S phase (space group Pnmm) [9]. After poling at RT, three dielectric anomalies T_1 , T_2 and T_3 are maintained, except for the fact that the intensity of T_3 peak is obviously enhanced owing to an electric field induced irreversible AFE/FE-FE phase transition. This influence can be further enhanced in the poled $x = 0.0025$ sample because it includes more amount of AFE phase at its virgin state (see Table 1). Although the AFE phase content in the virgin samples increases with further increasing x , yet the intensity of the dielectric peak at T_3 for poled samples gradually decreases probably owing to the increased reversibility of the AFE-FE phase transition. As $x \geq 0.005$, the disappearance of T_3 peak in the virgin sample indicated that it becomes a pure AFE P phase at RT. However, the T_3 peak still exists in the poled $0.005 \leq x \leq 0.01$ samples, suggesting that the part of AFE phase to FE phase transition is irreversible. By comparison, with increasing CZ content, the T_3 peak shifts to the low temperature side in the poled sample till it completely disappears as $x = 0.03$,

indicating that the AFE phase in the $x = 0.03$ sample is so stable that the electric field induced AFE to FE phase transition is reversible.

To further disclose the type and reversibility of the phase transition with changing x , the P-E, S-E loops and the corresponding polarization current density vs. electric field (J-E) curves measured during the first and second cycles for (0.94-x)NN-0.06BZ-xCZ ceramics are shown in Fig. 6. For the $x = 0$ ceramic, a square-shaped P-E loop before and after poling can be observed, further demonstrating a dominant FE phase at RT. From the change of its strain loop, one can believe that an irreversible field induced FE Q phase (including a slight amount of AFE P phase) to FE monoclinic phase transition occurs during loading. With increasing x , the amount of the polarization current peak during the first cycle changes from one (P_1) at $x = 0$ to two (P_1 and P_2) at $x = 0.0025$ because the AFE phase content in the virgin sample increases. The disappearance of P_1 peak in the virgin $x \geq 0.005$ sample indicates that it belongs to a pure AFE P phase, keeping consistency with the result in Fig. 5. The appearance of P_3 peak in the third quadrant in the $x \geq 0.01$ samples suggests that part of AFE phases start to be stable so that the field induced AFE to FE phase transition is reversible. Both the increase in the P_3 peak intensity and the decrease in the remanent polarization P_{r2} observed in the second cycle indicate that the AFE phase starts to become more and more stable with increasing x . The near-zero P_{r2} value observed in the $x = 0.03$ sample illustrates a reversible field induced AFE to FE phase transition, keeping a good agreement with the disappearance of T_3 phase in Fig. 5(f). This can be further illustrated by the change of negative strains observed in the second cycle. The existence of negative strains in the poled $x = 0.01$ sample accounts for the remaining FE phase after one electric cycle owing to irreversible AFE-FE phase transition. The S-E loops for the

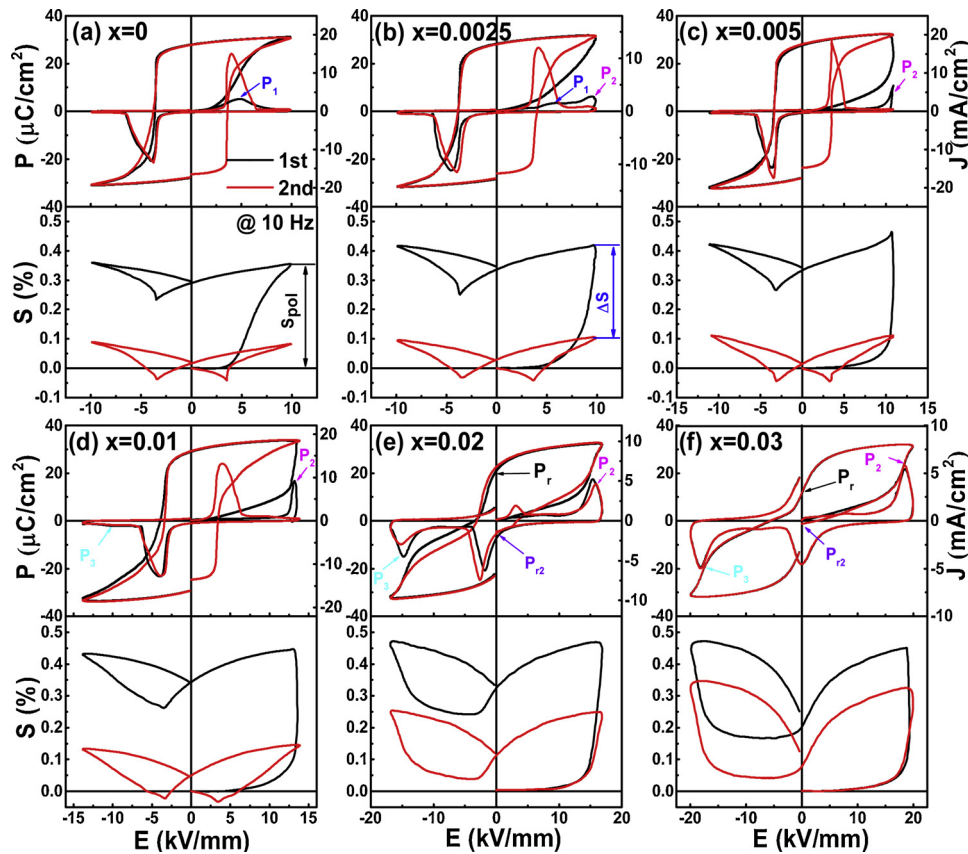


Fig. 6. P-E, S-E loops and the corresponding J-E curves at 10 Hz during the first and second electric cycles for (0.94-x)NN-0.06BZ-xCZ ceramics: (a) $x = 0$, (b) $x = 0.0025$, (c) $x = 0.005$, (d) $x = 0.01$, (e) $x = 0.02$ and (f) $x = 0.03$.

$x = 0.03$ sample before and after poling are still not repeated compared with the corresponding P-E loops, because the electric field induced FE monoclinic phase changes into a new AFE phase with a monoclinic symmetry rather than its initial AFE P phase after removal of the external field [22]. As a result, the substitution of CZ for NN tends to gradually stabilize the antiferroelectricity of the sample, accompanying a change from a dominant FE orthorhombic Q phase (including a few amount of AFE phase) at $x = 0$, to a pure AFE orthorhombic P phase with irreversible AFE-FE phase transition at $x = 0.005$ and finally into a pure AFE orthorhombic P phase with a reversible AFE-FE phase transition at $x = 0.03$.

The evolution of the maximum polarization P_{\max} , remanent polarization P_r , $P_{\max} - P_r$, the driving field of AFE-FE phase transition (E_{A-F}) at P_2 , the poling strain (S_{pol}) during the first electric field cycle, the strain difference (ΔS) between the first and second electric cycles and the quasi-static d_{33} as a function of x is summarized in Fig. 7. It can be seen that P_{\max} remains almost constant within the studied composition range owing to the generation of the similar FE phase under a strong external electric field irrespective of their initial states. Both P_r and d_{33} values keep constant with increasing x up to 0.01 and then rapidly decreases as $x < 0.01$, suggesting that the post-poled $x \leq 0.01$ samples exhibit an irreversible FE state, but the poled $x < 0.01$ samples have a reversible AFE state. As a result, a monotonous increase in $P_{\max} - P_r$ with increasing x denotes a weakening ferroelectricity ($0 \leq x \leq 0.005$) and an enhancing antiferroelectricity ($x \geq 0.01$). This change tendency can be also reflected by the variation of E_{A-F} . The increase of E_{A-F} with x indicates a more stable AFE state. Moreover, it can be seen that S_{pol} (as indicated in Fig. 6) first increases with x and arrives at a plateau at $x = 0.005$ because the amount of AFE phase becomes the most at $x = 0.005$. The ΔS value (as indicated in Fig. 6) is believed to originate from the irreversible process between the first and second cycles. It reaches the highest value at $x = 0.005$ because the $0 \leq x \leq 0.005$ samples experience a

transition from an irreversible FE-FE phase transition to an irreversible AFE-FE phase transition. The field induced AFE-FE phase transition is usually believed to have a relatively large strain contribution compared with the FE-FE phase transition owing to enhanced volume effects [30]. As $x < 0.01$, a rapid decrease of ΔS just corresponds to the enhancing stability of the AFE phase (or the reversibility of AFE-FE phase transition) with x .

In order to further clarify the evolution of the phase structure and the AFE stability, in-situ synchrotron XRD results of three representative compositions are shown in Fig. 8. A typical (100) doublet and a (110) triplet corresponding to an orthorhombic phase can be observed in the $x = 0$ virgin sample. When an external field of 8 kV/mm is applied, additional reflections corresponding to the monoclinic symmetry can be detected in both (100) and (110). The high-field FE monoclinic phase can be detected even after removal of the external electric field, confirming that the field induced FE/AFE orthorhombic to FE monoclinic phase transition is irreversible. An irreversible orthorhombic to monoclinic phase transition was also found in the $x = 0.005$ ceramic. The difference thing is that the initial orthorhombic phase in the $x = 0.005$ sample is an AFE in nature. The AFE orthorhombic phase in the $x = 0.03$ sample also changes into an FE monoclinic phase under 20 kV/mm. Though a monoclinic phase can be maintained after releasing the electric field, it should change from an FE state to an AFE state, considering the reversibility of AFE-FE phase in this sample. That is to say, the strain difference between the first and second cycles for the $x = 0.03$ sample (Fig. 6(f)) should be mainly caused by the difference in the phase structure of initial and final AFE phases although the AFE-FE phase transition is reversible.

A composition-electric field phase diagram is plotted in Fig. 9 according to the above analysis. For the virgin state, the phase structure gradually changes from a dominant FE orthorhombic Q phase to a pure AFE orthorhombic P phase ($x \geq 0.005$) with increasing x . When an

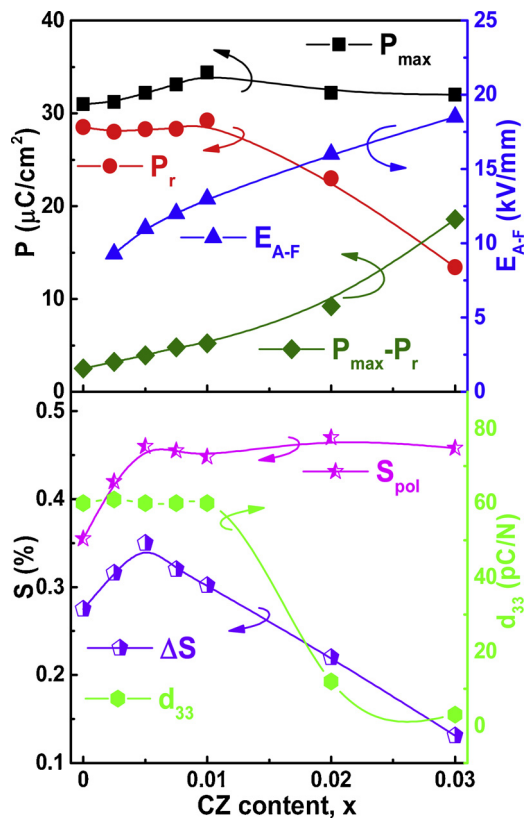


Fig. 7. The P_{max} , P_r , $P_{max}-P_r$, E_{A-F} , the S_{pol} achieved from the first electric field cycle, the ΔS values between the first and second electric field cycles, and d_{33} values as a function of CZ content.

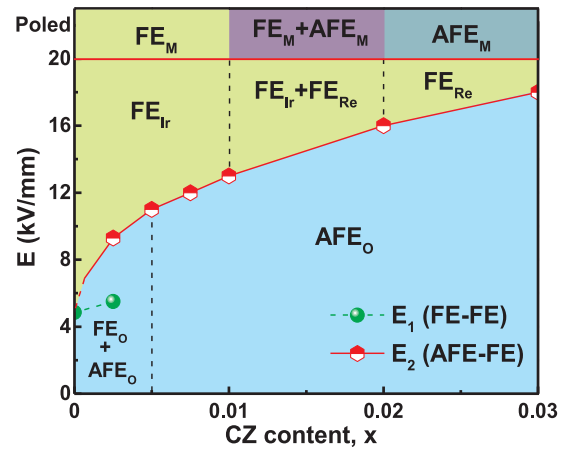


Fig. 9. Composition-electric field phase diagram of the $(0.94-x)NN-0.06BZ-xCZ$ ceramic upon loading and unloading electric fields (O: orthorhombic; M: monoclinic; Ir: irreversible; Re: reversible).

external electric field is applied, all compositions transform into an FE monoclinic phase above respective critical electric fields. This high-field induced FE phase can be maintained after poling only in the samples with $x \leq 0.01$, but can turn back to the AFE state at least partially for the compositions with $x > 0.01$, suggesting a gradual increase of the AFE stability with increasing CZ content.

4. Conclusions

The evolution of the AFE stability and the reversibility of AFE-FE phase transition with x was explored in $(0.94-x)NN-0.06BZ-xCZ$ lead-free ceramics. With the substitution of CZ for NN, the virgin phase structure gradually changes from a dominant FE orthorhombic Q phase in the $x = 0$ ceramic to a gradually stabilized AFE orthorhombic P phase in the $x \geq 0.005$ ceramics. The FE Q phase irreversibly transforms into an FE monoclinic phase during poling process. The AFE P phase also changes into an FE monoclinic phase under a high electric field, but the induced FE monoclinic phase gradually becomes unstable after removal of electric field with increasing x . A reversible AFE to FE phase transformation can be observed in the $x = 0.03$ ceramic although the initial and final AFE states before and after poling are still different. Our study would provide a solid fundament for further study of the NN-based lead-free AFE ceramics by means of a deep understanding of the law for tuning the AFE stability.

Acknowledgement

Financial support from the National Natural Science Foundation of China (Grant No. 51472069) is gratefully acknowledged.

References

- [1] W.Y. Pan, C.Q. Dam, Q.M. Zhang, L.E. Cross, Large displacement transducers based on electric field forced phase transitions in the tetragonal $(Pb_{0.97}La_{0.02})(Ti,Zr,Sn)O_3$ family of ceramics, *J. Appl. Phys.* 66 (1989) 6014.
- [2] F. Jona, G. Shirane, F. Mazzi, R. Pepinsky, X-Ray and neutron diffraction study of antiferroelectric lead zirconate, *PbZrO₃*, *Phys. Rev.* 105 (1957) 849–856.
- [3] A.K. Tagantsev, K. Vaideeswaran, S.B. Vakhrušev, A.V. Filimonov, R.G. Burkovsky, A. Shaganov, D. Andronikova, A.I. Rudskoy, A.Q.R. Baron, H. Uchiyama, D. Chernyshov, A. Bosak, Z. Ujma, K. Roleder, A. Majchrowski, J.-H. Ko, N. Setter, The origin of antiferroelectricity in $PbZrO_3$, *Nat. Commun.* 4 (2013) 2229.
- [4] A.S. Mischenko, Q. Zhang, J.F. Scott, R.W. Whatmore, N.D. Mathur, Giant electrocaloric effect in thin-film $PbZr_{0.95}Ti_{0.05}O_3$, *Science* 311 (2006) 1270–1271.
- [5] Z. Liu, T. Lu, J.M. Ye, G.S. Wang, X.L. Dong, R. Withers, Y. Liu, Antiferroelectrics for energy storage applications: a review, *Adv. Mater. Technol.* 3 (2018) 1800111.
- [6] H. Qi, R.Z. Zuo, Linear-like lead-free relaxor antiferroelectric $(Bi_{0.5}Na_{0.5})TiO_3-NaNbO_3$ with giant energy-storage density/efficiency and super stability against temperature and frequency, *J. Mater. Chem. A* (2019), <https://doi.org/10.1039/C8TA12232F>.

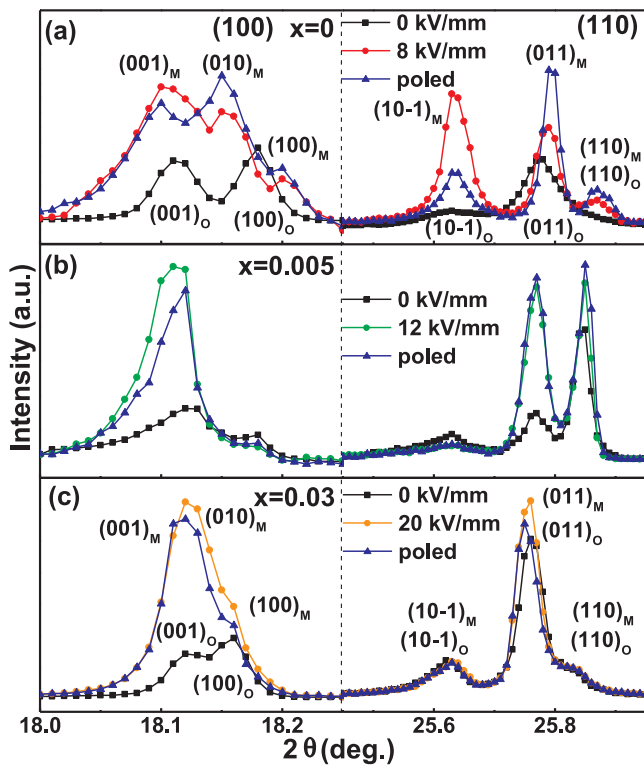


Fig. 8. Evolution of (100) and (110) diffraction lines of synchrotron XRD under different electric loading conditions for samples with (a) $x = 0$, (b) $x = 0.005$ and (c) $x = 0.03$.

- [7] A.C. Sakowski-Cowley, K. Lukaszewicz, H.D. Megaw, The structure of sodium niobate at room temperature, and the problem of reliability in pseudosymmetric structures, *Acta Crystallogr. B* 25 (1969) 851–865.
- [8] A.M. Glazer, H.D. Megaw, Studies of the lattice parameters and domains in the phase transitions of NaNbO_3 , *Acta Cryst. A* 29 (1973) 489–495.
- [9] S.K. Mishra, N. Choudhury, S.L. Chaplot, P.S.R. Krishna, R. Mittal, Competing antiferroelectric and ferroelectric interactions in NaNbO_3 : Neutron diffraction and theoretical studies, *Phys. Rev. B* 76 (2007) 024110.
- [10] L. Jiang, D.C. Mitchell, W. Dmowski, T. Egami, Local structure of NaNbO_3 : a neutron scattering study, *Phys. Rev. B* 88 (2013) 014105.
- [11] Y.I. Yuzyuk, P. Simon, E. Gagarina, L. Hennet, D. Thiaudière, V.I. Torgashev, S.I. Raevskaya, I.P. Raevskii, L.A. Reznitchenko, J.L. Sauvajol, Modulated phases in NaNbO_3 : raman scattering, synchrotron x-ray diffraction, and dielectric investigations, *J. Phys. Condens. Matter* 17 (2005) 4977–4990.
- [12] S.K. Mishra, R. Mittal, V.Yu. Pomjakushin, S.L. Chaplot, Phase stability and structural temperature dependence in sodium niobate: A high-resolution powder neutron diffraction study, *Phys. Rev. B* 83 (2011) 134105.
- [13] L.E. Cross, Electric double hysteresis in $(\text{K}_x\text{Na}_{1-x})\text{NbO}_3$ single crystals, *Nature* 181 (1958) 178–179.
- [14] Y.I. Yuzyuk, R.A. Shakhovoy, S.I. Raevskaya, I.P. Raevskii, M.E. Marssi, M.G. Karkut, P. Simon, Ferroelectric Q-phase in a NaNbO_3 epitaxial thin film, *Appl. Phys. Lett.* 96 (2010) 222904.
- [15] J. Koruza, P. Groszewicz, H. Breitzke, G. Buntkowsky, T. Rojac, B. Malič, Grain-size-induced ferroelectricity in NaNbO_3 , *Acta Mater.* 126 (2017) 77–85.
- [16] R. Jiménez, M.L. Sanjuán, B. Jiménez, Stabilization of the ferroelectric phase and relaxor-like behaviour in low Li content sodium niobates, *J. Phys. Condens. Matter* 16 (2004) 7493–7510.
- [17] R.A. Shakhovoy, S.I. Raevskaya, L.A. Shakhovaya, D.V. Suzdalev, I.P. Raevskii, Y.I. Yuzyuk, A.F. Semenchov, M.E. Marssi, Ferroelectric Q and antiferroelectric P phases' coexistence and local phase transitions in oxygen-deficient NaNbO_3 single crystal: micro-Raman, dielectric and dilatometric studies, *J. Raman Spectrosc.* 43 (2012) 1141–1145.
- [18] H.Z. Guo, H. Shimizu, C.A. Randall, Direct evidence of an incommensurate phase in NaNbO_3 and its implication in NaNbO_3 -based lead-free antiferroelectrics, *Appl. Phys. Lett.* 107 (2015) 112904.
- [19] H.Y. Ge, Y.D. Hou, C. Xia, M.K. Zhu, H. Wang, H. Yan, Preparation and piezoelectricity of NaNbO_3 high-density ceramics by molten salt synthesis, *J. Am. Ceram. Soc.* 94 (2011) 4329–4334.
- [20] H. Shimizu, K. Kobayashi, Y. Mizuno, C.A. Randall, Advantages of low partial pressure of oxygen processing of alkali niobate: NaNbO_3 , *J. Am. Ceram. Soc.* 97 (2014) 1791–1796.
- [21] L.M. Chao, Y.D. Hou, M.P. Zheng, M.K. Zhu, High dense structure boosts stability of antiferroelectric phase of NaNbO_3 polycrystalline ceramics, *Appl. Phys. Lett.* 108 (2016) 212902.
- [22] R.Z. Zuo, J. Fu, H. Qi, Stable antiferroelectricity with incompletely reversible phase transition and low volume-strain contribution in BaZrO_3 and CaZrO_3 substituted NaNbO_3 ceramics, *Acta Mater.* 161 (2018) 352–359.
- [23] H. Shimizu, H.Z. Guo, S.E. Reyes-Lillo, Y. Mizuno, K.M. Rabe, C.A. Randall, Lead-free antiferroelectric: $x\text{CaZrO}_3$ -(1-x) NaNbO_3 system ($0 \leq x \leq 0.10$), *Dalton Trans.* 44 (2015) 10763–10772.
- [24] H.Z. Guo, H. Shimizu, Y. Mizuno, C.A. Randall, Strategy for stabilization of the antiferroelectric phase (Pbma) over the metastable ferroelectric phase (P2₁ma) to establish double loop hysteresis in lead-free (1-x) NaNbO_3 -x SrZrO_3 solid solution, *J. Appl. Phys.* 117 (2015) 214103.
- [25] L.S. Gao, H.Z. Guo, S.J. Zhang, C.A. Randall, A perovskite lead-free antiferroelectric $x\text{CaHfO}_3$ -(1-x) NaNbO_3 with induced double hysteresis loops at room temperature, *J. Appl. Phys.* 120 (2016) 204102.
- [26] M.X. Dou, J. Fu, R.Z. Zuo, Electric field induced phase transition and accompanying giant poling strain in lead-free NaNbO_3 - BaZrO_3 ceramics, *J. Eur. Ceram. Soc.* 38 (2018) 3104–3110.
- [27] Y.H. Xu, W. Hong, Y.J. Feng, X.L. Tan, Antiferroelectricity induced by electric field in NaNbO_3 -based lead-free ceramics, *Appl. Phys. Lett.* 104 (2014) 052903.
- [28] K.E. Johnston, C.C. Tang, J.E. Parker, K.S. Knight, P. Lightfoot, S.E. Ashbrook, The polar phase of NaNbO_3 : a combined study by powder diffraction, solid-state NMR, and first-principles calculations, *J. Am. Chem. Soc.* 132 (2010) 8732–8746.
- [29] Y.I. Yuzyuk, E. Gagarina, P. Simon, L.A. Reznitchenko, L. Hennet, D. Thiaudière, Synchrotron x-ray diffraction and Raman scattering investigations of $(\text{Li}_x\text{Na}_{1-x})\text{NbO}_3$ solid solutions: evidence of the rhombohedral phase, *Phys. Rev. B* 69 (2004) 144105.
- [30] S.E. Park, M.J. Pan, K. Markowski, S. Yoshikawa, L.E. Cross, Electric field induced phase transition of antiferroelectric lead lanthanum zirconate titanate stannate ceramics, *J. Appl. Phys.* 82 (1997) 1798–1803.